

Joint DOA and Frequency Estimation Method of Multiband Signals With Single Optical Frequency Comb

Yichen Wang^{ID}, Rongguang Feng^{ID}, Shenda Zhang^{ID}, Shuguo Xie^{ID}, Senior Member, IEEE, and Yan Yang^{ID}

Abstract—Traditional electromagnetic signal receiving techniques require high Nyquist sampling rates, making it difficult to achieve rapid frequency and direction of arrival (DOA) estimation for multiple noncooperative signals over a wide bandwidth. Optical frequency comb (OFC) based sampling reception techniques can simultaneously down-convert multiband signals into the same low frequency region, thus addressing this challenge. However, due to the under-sampling process, the original frequency information is lost, further rendering the phase information unavailable. To overcome these limitations, this article proposes a single OFC driven, optical delay controlled uniform linear array (ULA) signal reception architecture. By introducing different lengths of optical fiber delay before each antenna channel, the proposed system enables joint carrier frequency and DOA estimation of multiband signals under sub-Nyquist sampling conditions. The method constructs a virtual array in the frequency domain using the autocorrelation matrix, and jointly solves for the down-converted frequency index and the DOA. It features high phase accuracy, low sampling complexity, and strong adaptability to wideband signals, while avoiding the increased system complexity and interchannel matching difficulties associated with existing multicomb sampling techniques. Simulation results show that within the 0–9.8 GHz range, the proposed system achieves a frequency estimation error of 3 kHz and an angular error of 0.67°. Experimental measurements demonstrate an average frequency estimation accuracy of 50 kHz and an average DOA estimation accuracy of 0.7°.

Index Terms—Direction of arrival (DOA) estimation, frequency recovery, optical frequency comb (OFC), sensor arrays.

I. INTRODUCTION

WITH the continuous advancement of electronic technology, the spectral components in the electromagnetic environment have become increasingly complex. To rapidly and reliably monitor the activities of primary users, fully utilize spectrum resources, and improve spectrum efficiency, broadband spectrum sensing has emerged as a critical task in both civilian and defense applications. Spectrum sensing

Received 11 October 2025; revised 17 November 2025; accepted 18 December 2025. Date of publication 20 January 2026; date of current version 2 February 2026. This work was supported by the National Natural Science Foundation of China under Grant 62401034. The Associate Editor coordinating the review process was Dr. Marco Faifer. (*Corresponding author: Yan Yang*)

Yichen Wang, Rongguang Feng, Shuguo Xie, and Yan Yang are with the Department of Electronic and Information Engineering, Beihang University, Beijing 100191, China (e-mail: wangyichen@buaa.edu.cn; yan@buaa.edu.cn).

Shenda Zhang is with the National Key Laboratory of Microwave Imaging, Aerospace Information Research Institute, Chinese Academy of Sciences, Beijing 100094, China.

Digital Object Identifier 10.1109/TIM.2026.3655889

requires the rapid acquisition of key signal features, such as amplitude, carrier frequency, and direction of arrival (DOA). However, the modern electromagnetic spectrum is characterized by wide frequency distribution (ranging from hundreds of megahertz to tens of gigahertz), a large number of signals, and strong noncooperativity. Direct signal sampling must comply with the Nyquist sampling theorem, which is impractical for devices tasked with sensing gigahertz-wide spectral ranges.

To overcome the sampling rate bottleneck in the field of spectrum sensing, several novel receiver system architectures have been proposed, such as sub-Nyquist sampling receivers in the electronic domain and optically undersampled microwave photonic receivers. In addition, algorithmic approaches such as compressed sensing (CS) and subspace algorithms, which align with these system structures, have also been developed.

Sub-Nyquist sampling methods, such as the oversampling method [1] and the Modulated Wideband Converter (MWC) [2], [3], [4], employ multipath parallelism and low-rate sampling to enable the system to reconstruct the original signal while sampling at a rate far below the highest frequency component. This significantly reduces the complexity of data acquisition and processing. However, classical DOA estimation techniques, including MUSIC [5], estimation of signal parameters via rotational invariance techniques (ESPRITs) [6], and sparse representation based methods [7], [8], [9], require prior knowledge of signal frequencies and thus cannot be directly applied under under-sampling conditions. To overcome this limitation, studies [10], [11], [12], [13] have designed special array structures (such as L-shaped arrays, symmetric uniform linear arrays (ULAs), 2-D coprime sampling architecture) and extended conventional algorithms to jointly estimate frequency and DOA from sub-Nyquist samples. One line of work leverages CS, assuming both parameters lie on predefined grids, to achieve simultaneous recovery. Another extends ESPRIT to 2-D settings, performing singular value decomposition (SVD) on multiple cross correlation matrices to estimate and automatically pair the parameters. Other studies [14], [15], [16], [17], [18] employ delay channels at each sensor, calculate cross correlation matrices with distinct time lags, and recover parameters using parallel factor analysis (PARAFAC) decomposition or extended ESPRIT. Despite their algorithmic advances, the reliance on complex array structures poses challenges for hardware implementation, limiting the practical deployment of sub-Nyquist joint estimation techniques.

Microwave photonic schemes [19], [20], [21], [22], [23], [24], [25], [26], which offer advantages such as instantaneous bandwidth, fast response, and electromagnetic interference (EMI) resistance, have attracted considerable attention from researchers. Among these schemes, receivers based on optical frequency combs (OFCs) provide a new solution for broadband spectrum sensing. An OFC consists of a series of uniformly spaced spectral lines. When this frequency comb is mixed with an RF signal, the high-frequency RF signal is down-converted to the first Nyquist zone, allowing to capture the entire time-domain information of the RF signal, including amplitude and phase, using an analog-to-digital converter (ADC) with a lower sampling rate. The main advantage of this technique is the significant reduction in measurement time and sampling equipment costs. However, the issue with single OFC is the loss of frequency information after subsampling, which has led to considerable academic attention and research.

In receiver systems based on OFC architectures, researchers have extensively investigated methods for estimating key parameter such as the RF signal's frequency. Several studies [27], [28], [29], [30], [31] have explored frequency measurement techniques using two optical sources with distinct repetition rates. By shifting the RF signal to different intermediate frequency (IF) bands via these sources, the frequency can be inferred based on its relative position to the comb lines. However, the dual-source system remains susceptible to measurement dead zones, especially when analyzing high-frequency or multifrequency signals. To overcome this limitation, Yang et al. [32] further proposed a triple-source OFC system capable of continuous, dead-zone-free frequency measurements. Nevertheless, increasing the number of OFCs significantly raises system complexity. More recently, Wang et al. [33] designed an asymmetric dual-branch electrooptic modulation system that introduces a controllable phase offset using a single OFC, enabling frequency estimation through phase-frequency mapping with reduced hardware complexity.

OFCs have also been adopted for joint frequency and DOA estimation [34]. Li et al. [34] proposed a scheme in which two optical pulse sequences with different repetition rates are combined via an optical coupler. Two antennas are placed at a fixed distance, and the received signals are loaded onto the two arms of a Mach-Zehnder modulator (MZM). By integrating optical pulse trains of different periods, the system performs subsampling of unknown RF signals and computes the phase difference between channels, enabling frequency measurements over the range of 0.5–40 GHz and phase shift detection up to $\pm 180^\circ$. However, dual-comb based frequency and DOA estimation systems suffer from the following limitations.

- 1) *Accuracy*: In systems that rely solely on the phase difference between two channels, phase jitter and link noise can significantly degrade measurement accuracy.
- 2) *Interference*: When multiple signals are input, the dual-comb system generates twice as many IF signals within the first Nyquist zone. To accurately distinguish the signals, precise control of the power difference between the two optical pulse sequences is required.

- 3) *Matching*: Although this power-based matching strategy is effective in single-signal measurements, as the number of signal sources increases, the probability of matching errors also rises, thereby reducing system robustness.

To address the issues mentioned above, this article proposes an optical delay linear array system based on a single OFC, which uses only one OFC and an adjustable optical delay line for parameter estimation. By employing multiple branch sensors with different time delays to form a ULA, we introduce a parameter estimation algorithm based on delayed sparse array elements, which estimates the frequency and DOA of multiband signals from optical under-sampling samples. The advantages of our system architecture are as follows.

- 1) Simulation results show that the system supports joint frequency and DOA estimation over the range of 0–9.8 GHz. When the signal-to-noise ratio (SNR) exceeds 0 dB, the frequency estimation error is approximately 3 kHz and the DOA estimation is performed within 0° – 180° , with an angular error of 0.67° . Experiments were conducted over the frequency range of 0.1–9.8 GHz, and the results indicate that the system achieves an average frequency estimation error of 50 kHz, and an average angular estimation error of 0.7° . Moreover, the system supports simultaneous measurements of multiple signals.
- 2) Our architecture uses only one OFC, which reduces cost while achieving robust noise resistance.
- 3) The proposed algorithm not only solves the frequency loss and measurement dead zone issues resulting from down-conversion with a single OFC but also automatically pairs the estimated parameters for multiple signals. This significantly reduces the computational complexity required for matching and avoids signal matching errors.

The structure of this article is as follows. Section II introduces the proposed receiver architecture and the received signal model; Section III describes the parameter estimation algorithm; Sections IV and V presents the simulation and experimental results; and Section VI concludes the article.

II. SYSTEM ARCHITECTURE

A. Proposed Receiver Architecture

We propose a joint parameter estimation algorithm using a virtual array based on optical time delay.

The proposed receiver architecture is illustrated in Fig. 1. First, an OFC is used to generate a pulsed optical sequence, which is then split by a planar lightwave circuit (PLC) splitter to ensure that each branch receives optical pulses with identical and synchronized repetition rates. The optical signals are then passed through fiber delay lines, introducing different time delays before being fed into each receiving channel. The M receiving channels, each consisting of an antenna and a MZM, are arranged in a ULA configuration. Here, the MZM provides the input port for the RF signal, modulating it onto the optical pulse train to generate replicas in different repetition frequency intervals. The replicas are converted to the electrical domain and low-pass filtered to retain only the IF components within the first repetition frequency range, thereby enabling the

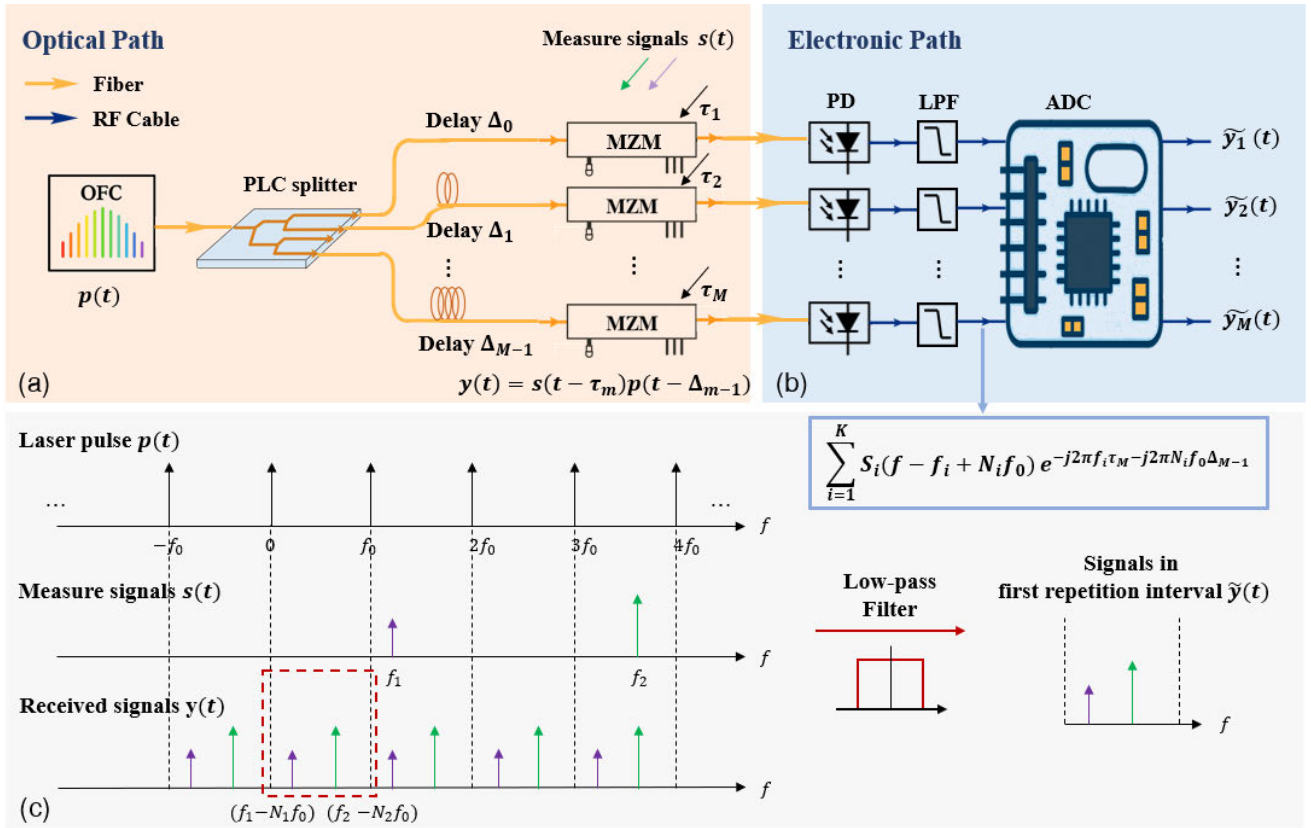


Fig. 1. System architecture. (a) Optical path. (b) Electronic path. (c) Signal model. OFC: optical frequency comb; MZM: Mach–Zehnder modulator; PLC splitter: planar lightwave circuit splitter; PD: photodetector; LPF: low-pass filter; and ADC: analog–digital converter.

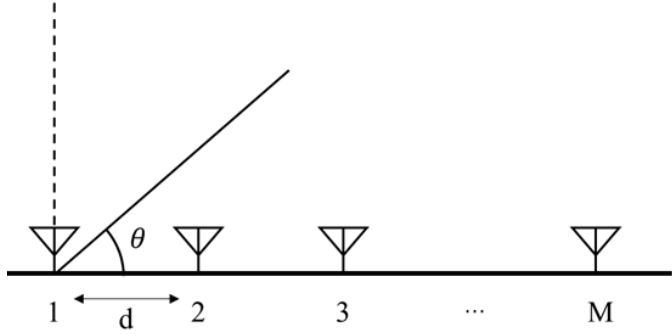


Fig. 2. Incident signal model.

OFC-based under-sampling measurement. The carrier frequency and DOA of the RF signals can be calculated based on the frequency and phase information of the multichannel IF signals. In this article, we first introduce the signal reception model under the ULA structure, followed by a detailed explanation of the under-sampling scheme and the design of its delay structure.

B. Signal Model

Assume there are K uncorrelated far-field narrowband sources spreading over a large bandwidth impinging on a wideband ULA with M receiving antennas separated by a distance d , as shown in Fig. 2.

Let $x_m(t)$ be the combination of K received signals observed in the time domain by the m th sensor. With the narrowband

assumption on the transmission sources $s(t)$, $x_m(t)$ can be expressed as

$$\begin{aligned} x_m(t) &= \sum_{i=1}^K s_i(t - \tau_m) + n_m(t) \\ &\approx \sum_{i=1}^K s_i(t) e^{-j2\pi f_i \tau_m} + n_m(t) \end{aligned} \quad (1)$$

where $n_m(t)$ represents the additive Gaussian noise of m th channel. The Fourier transform of $x_m(t)$ is given by

$$X_m(f) = \sum_{i=1}^K S_i(f - f_i) e^{-j2\pi f_i \tau_m} + N_m(f) \quad (2)$$

where f_i represents carrier frequency, τ_m , which depends on the unknown incident angle $\theta_i \in [0, \pi]$, denotes the time delay between the first and m th channel

$$\tau_m = \frac{(m-1)d \cos(\theta_i)}{c} \quad (3)$$

where c is the speed of light.

We make the following assumptions regarding the source signal.

- 1) The multiband signal is bandlimited to $[0, f_{NYQ}]$, where the Nyquist frequency f_{NYQ} is defined as the highest frequency of the incident signal.
- 2) The K source signals, distributed over a wide frequency band, are narrowband signals, each with a bandwidth not exceeding the repetition frequency interval of the OFC.

- 3) To distinguish between the two incoming signals, we require that $(f_i, \theta_i) \neq (f_j, \theta_j)$, with $i \neq j$.
- 4) To avoid direction-finding ambiguity, we require the highest frequency $f_{\text{NYQ}} = c/\lambda_{\text{NYQ}}$ and the antenna distance d to satisfy the following relationship: $d \leq \lambda_{\text{NYQ}}/2$.

C. Optical Under-Sampling Measurement

As described in [31], the impulse string of the OFC is evaluated as

$$p(t) = \sum_{n=-\infty}^{+\infty} e^{jn2\pi f_0 t} \quad (4)$$

where f_0 is the repetition frequency of the OFC. In each sensor, the received signal $x(t)$ is mixed with the optical pulse string $p(t)$. The Fourier transform of $y_m(t) = x_m(t)p(t)$, which becomes a frequency-shifted version of the input signal, can be expressed as

$$Y_m(f) = \sum_{n=-\infty}^{+\infty} X(f - n f_0). \quad (5)$$

Apply low-pass filtering to $Y_m(f)$. The cut-off frequency range of this filter is defined as $\mathcal{F}_s = [-f_0/2, f_0/2]$, which is carefully chosen to retain only the signals within the first repetition frequency range, in the following equation:

$$Y'_m(f) = \begin{cases} X(f - N f_0), & f \in \mathcal{F}_s \\ 0, & f \notin \mathcal{F}_s. \end{cases} \quad (6)$$

Substituting (2) into (6), we have

$$Y'_m(f) = \sum_{i=1}^K S_i(f - f_i + N_i f_0) e^{-j2\pi f_i \tau_m} + N_m(f) \quad (7)$$

where $N_i = \text{fix}[f_i/f_0]$, with fix denoting the rounding-down function. To be more specific, the high frequency signals are down-converted to each beat frequency interval. As shown in Fig. 1, the N_i th replica falls in the first repetition frequency range, which allows a low-speed ADC to acquire the complete information of the replica in a single capture, including the phase difference introduced by (1). However, because the RF carrier frequency is folded during the down-conversion, this phase difference cannot be directly used. It contains two coupled unknown parameters, the carrier frequency f_i and the DOA θ_i . To jointly and simultaneously estimate these coupled parameters, we introduce an optical delay strategy that provides an additional variable, enabling both f_i and θ_i to be determined.

It should be noted that the above derivations are based on the complex harmonic form. For the signal in the actual system, which includes both positive frequency and mirror-negative frequency, the down-converted signal becomes

$$\widetilde{Y}_m(f) = \sum_{i=1}^K [S_i(f - f_i + N_i f_0) e^{-j2\pi f_i \tau_m} + S_i(f + f_i - N_i f_0) e^{j2\pi f_i \tau_m}] + N_m(f). \quad (8)$$

Therefore, we will also discuss the impact of $\pm N_i$ in the frequency recovery process in Section III.

D. Optical Delay Strategy

For the convenience in derivation, we assume that the source signal $s(t)$ has a complex harmonic form: $e^{-j2\pi f_s t}$. Thus, the output of m th sensor in (7) can be rewritten as

$$y_m(t) = \sum_{i=1}^K e^{-j2\pi(f_i - N_i f_0)t - j2\pi f_i \tau_m} + n_m(t). \quad (9)$$

Let $f_{r,i}$ be the frequency of i th down-converted signal, which is measurable in the spectrum. According to (9), f_i can be recovered by

$$f_i = f_{r,i} + N_i f_0. \quad (10)$$

Through (10), we transform the problem of finding the carrier frequency f_i into the problem of finding N_i . In order to find the value of N_i , different extra time delay Δ is added to each optical path before the electro-optical modulator and antenna. It means that the pulse train $p(t)$ in (4) must be replaced by $p(t - \Delta_{m-1})$, and consequently the output expression in (9) needs to be rewritten as

$$y_m(t) = \sum_{i=1}^K e^{-j2\pi(f_i - N_i f_0)t - j2\pi f_i \tau_m - j2\pi N_i f_0 \Delta_{m-1}} + n_m(t). \quad (11)$$

Comparing with (1), we propose that (11) is the array signal reception model after time-delay and under-sampling processing. Rewriting it in matrix form

$$\mathbf{Y} = \mathbf{AS} + \mathbf{N} \quad (12)$$

where $\mathbf{S} = [s_1(t) \ s_2(t) \ \dots \ s_K(t)]^T$, and array manifold matrix \mathbf{A} can be expressed as an $M \times K$ matrix

$$\begin{bmatrix} 1 & \dots & 1 \\ e^{-j2\pi f_1 \tau_{11} - j2\pi N_1 f_0 \Delta_1} & \dots & e^{-j2\pi f_K \tau_{1K} - j2\pi N_K f_0 \Delta_1} \\ \vdots & \ddots & \vdots \\ e^{-j2\pi f_1 \tau_{M1} - j2\pi N_1 f_0 \Delta_{M-1}} & \dots & e^{-j2\pi f_K \tau_{MK} - j2\pi N_K f_0 \Delta_{M-1}} \end{bmatrix}. \quad (13)$$

This reception architecture introduces a term that contains only frequency components through time delay. It is important to note that the delay value differs for each channel. Therefore, by appropriately selecting the delay values, the desired frequency and DOA can be obtained correctly.

III. PARAMETER ESTIMATION PRINCIPLE

A. Carrier Frequency and DOA Estimation

After implementing the hardware architecture, we provide an algorithm for estimating parameters N and θ .

From (10), it is evident that since we need to estimate the subband index N_i and baseband frequency $f_{r,i}$ simultaneously and match them to compute and recover the original frequency, transforming the received signal into the frequency domain for calculation would be a better choice. For now, we only consider the case where each frequency point does not overlap after under-sampling.

Firstly, perform a Fourier transform on received data \mathbf{Y} . For any channel, considering $k = 1, \dots, K$, conduct peak search on the result after fast Fourier transform (FFT), and record the peak value and corresponding frequency point coordinates. For the other channels, extract the complex values

at the corresponding positions based on the frequency point coordinates to form the respective data vectors

$$\mathbf{y}(f_k) = \mathbf{A}(f_k)\mathbf{S}(f_k) + \mathbf{N}(f_k). \quad (14)$$

Equation (14) is referred to as frequency domain snapshot vectors, where $\mathbf{S}(f_k)$ is the output vector of signals in the frequency domain. And $\mathbf{N}(f_k)$ is the output vector of noise in the frequency domain.

Examining the auto-correlation matrix of the received signals

$$\begin{aligned} \mathbf{R} &= E[\mathbf{y}\mathbf{y}^H] = \mathbf{A}\mathbf{R}_s\mathbf{A}^H + \sigma^2\mathbf{I} \\ &= \sum_{k=1}^K p_k a(\theta_k) a(\theta_k)^H \end{aligned} \quad (15)$$

where $\mathbf{R}_s = E[\mathbf{S}\mathbf{S}^H] = \text{diag}(p_1, \dots, p_K)$ is the signal correlation matrix, which is a diagonal matrix whose elements represent the power of signals.

We assume that the frequency points after down-conversion do not overlap, under which condition only one signal is processed at each frequency point, leading to $K = 1$. Substituting the matrix from (13) to (15) and simplifying, we obtain the (m, n) entry of this auto-correlation matrix

$$R_{mn} = p_k e^{-j2\pi f_k(m-n)d \cos(\theta_k)/c - j2\pi N_k f_0(\Delta_{m-1} - \Delta_{n-1})}. \quad (16)$$

Extract the following terms to form a new matrix:

$$\begin{aligned} \mathbf{X}_R &= \begin{bmatrix} R_{21} \\ R_{32} \\ \vdots \\ R_{M(M-1)} \end{bmatrix} \\ &= p_k \begin{bmatrix} e^{-j2\pi f_k d \cos(\theta_k)/c - j2\pi N_k f_0 \Delta_1} \\ e^{-j2\pi f_k d \cos(\theta_k)/c - j2\pi N_k f_0 (\Delta_2 - \Delta_1)} \\ \vdots \\ e^{-j2\pi f_k d \cos(\theta_k)/c - j2\pi N_k f_0 (\Delta_{M-1} - \Delta_{M-2})} \end{bmatrix}. \end{aligned} \quad (17)$$

By extracting the constants $C_k = e^{-j2\pi f_k d \cos(\theta_k)/c}$, a new vector with the subband index N as the variable is formed

$$\boldsymbol{\beta}(N_k) = \begin{bmatrix} e^{-j2\pi N_k f_0 \Delta_1} \\ e^{-j2\pi N_k f_0 (\Delta_2 - \Delta_1)} \\ \vdots \\ e^{-j2\pi N_k f_0 (\Delta_{M-1} - \Delta_{M-2})} \end{bmatrix}. \quad (18)$$

In (18), a virtual baseline based on optical domain delay is constructed. Equation (17) is rearranged into a vector product form, as shown in (19). We observe that the form of the equation is similar to a single snapshot reception vector. At this point, any suitable subspace algorithm can be used to recover N from the matrix, and we use the MUSIC algorithm for processing

$$\mathbf{X}_R = \boldsymbol{\beta}(N_k) C_k p_k. \quad (19)$$

The MUSIC algorithm is employed for subsequent calculations, and by traversing the subband index N , the down-conversion number can be determined

$$P = \frac{1}{\boldsymbol{\beta}(N)^H \mathbf{U}_N \mathbf{U}_N^H \boldsymbol{\beta}(N)} \quad (20)$$

where \mathbf{U}_N is the noise matrix of \mathbf{X}_R , which contains $M - P$ eigenvectors corresponding to noises.

As mentioned in Section II, real-world incident signals have negative image frequencies, so during calculations, N is traversed starting from negative values. If the final result is positive, it corresponds to a positive frequency; otherwise, it corresponds to a negative frequency. The carrier frequency is then recovered according to the following formula:

$$f = \begin{cases} f_r + N f_0, & N \geq 0 \\ |N| f_0 - f_r, & N < 0. \end{cases} \quad (21)$$

After determining the carrier frequency f_k , we now discuss how to estimate DOA from the matrix \mathbf{X}_R . Write $z = r e^{j\phi}$, and define $\angle(z) = \text{mod}(\phi, 2\pi)$ where $\text{mod}(x, y)$ is a modulo operator which returns the remainder of division of x by y . We have

$$\theta_k = \cos^{-1} \left(-\frac{c}{2\pi f_k d} \angle(C_k) \right). \quad (22)$$

Since the calculations are performed at each frequency point in the frequency domain, there is an inherent matching relationship between the frequency and DOA, eliminating the need for further processing.

B. Choice of Parameters

To avoid frequency estimation ambiguity, we make the following assumptions regarding the delay factor:

$$\Delta < \frac{1}{2f_0 N_{\max}} \quad (23)$$

where $N_{\max} = \text{fix}[f_{\text{NYQ}}/f_0]$, which represents the down-mixing count corresponding to the highest frequency measurable by the system.

The following is the derivation of this assumption. We set $N_i, N_j \in [-N_{\max}, N_{\max}]$. In spatial spectrum estimation, the ambiguity condition can be expressed as

$$\beta(N_i) = C \beta(N_j) \quad (24)$$

where C is a constant. Rewrite (24) in the following form:

$$\frac{\beta(N_i)}{\beta(N_j)} = \frac{e^{-j2\pi N_i f_0 \Delta}}{e^{-j2\pi N_j f_0 \Delta}} = C \quad (25)$$

which can be expressed as

$$2\pi (N_i - N_j) f_0 \Delta = 2n\pi, \quad n \in \mathbb{Z}. \quad (26)$$

It is evident that the ambiguity-free condition can be written as

$$\Delta < \frac{1}{\max |N_i - N_j| f_0} < \frac{1}{2f_0 N_{\max}}. \quad (27)$$

The upper bound of the measurable range is given by (27), which indicates that a smaller Δ leads to a wider ambiguity-free frequency measurement range. However, a smaller delay step also amplifies the system's sensitivity to noise and phase fluctuations. To quantitatively examine this effect, we further conduct Monte-Carlo simulations to evaluate the estimation errors under different Δ values. The resulting curves are shown in Fig. 3. When Δ is small, the phase shift introduced by the

TABLE I
COMPUTATIONAL COMPLEXITIES OF VARIOUS ALGORITHMS

Ref	Algorithm	Main Process	Computational Complexity
[15]	CP-PASS-FD (PARAFAC)	Cross-correlation, CP decomposition, Parameter estimation	$O(C_p(M^2KT + MKT + M^2K))$
[18]	BSS-DOA-CS (CS)	CTF [1], RA-ORMP, Signal reconstruction	$O(N_\delta N_r(NM^2K + NMK^2) + M^2T)$
[18]	BSS-DOA-SD (MUSIC)	CTF [1], MUSIC, Signal reconstruction	$O(N_s N_r NM^2 + MKT + M^2T)$
This work	Proposed method (MUSIC)	Covariance, EVD, Parameter estimation	$O(K(M^3 + NM^2) + MT \log T)$

Parameter definitions: M : array elements; K : signal sources; T : number of snapshots; N : number of sub-bands; C_p : ALS iterations in CP decomposition; N_r : grid points used in the grid refinement process; N_δ : number of refinement iterations.

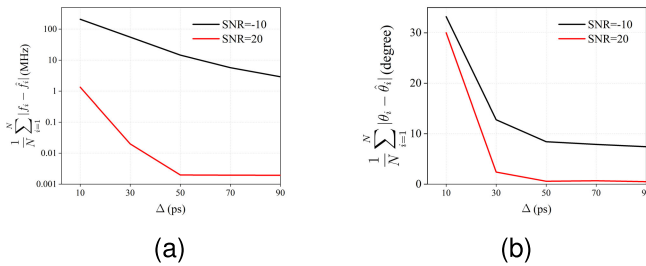


Fig. 3. Influence of the delay step size in the proposed method. (a) Frequency estimation performance. (b) DOA estimation performance.

delay line becomes insufficient, reducing the phase discrimination between different signals. As a result, noise dominates a larger portion of the phase term, leading to increased frequency and DOA estimation errors. Although a smaller Δ provides a wider ambiguity-free frequency measurement range, it also becomes more sensitive to noise. Considering this trade-off, we select $\Delta = 50\text{ ps}$ for the subsequent simulations and experiments.

C. Computational Complexity

This section compares the computational complexity of the proposed method with several representative algorithms, including PARAFAC, CS, and subspace-based approaches. The results are summarized in Table I, where only the dominant computational terms are listed and lower-order terms are omitted.

As shown in Table I, PARAFAC requires multiple alternating least-squares (ALS) updates during CP decomposition. Its complexity grows significantly with the number of snapshots T and the iteration count C_p . CS method performs sparse reconstruction and joint estimation on a 2-D angle-frequency grid, where the computational cost is dominated by large scale matrix multiplications and the grid size. In contrast, subspace-based blind spectrum sensing and DOA estimation algorithm based on subspace decomposition (BSS-DOA-SD) requires only a single eigenvalue decomposition (EVD) but still conducts a 2-D MUSIC search, causing its complexity to scale rapidly with the grid resolution.

The proposed method operates fundamentally differently. It constructs the covariance matrix using single-frequency snapshots and completes joint frequency and DOA estimation via one EVD and a 1-D subband index search. This avoids both the 2-D pseudospectrum search and the iterative optimization commonly required by the aforementioned algorithms.

The overall complexity is dominated by $O(K(M^3 + NM^2))$, while the FFT preprocessing term $O(MT \log T)$ can be efficiently parallelized in hardware implementations, rendering the impact of a large snapshot number T negligible in real-time applications. Furthermore, by performing estimation in the frequency domain, the proposed method decouples computational complexity from grid size, achieving high estimation accuracy while substantially reducing computational load.

D. Comparison With Existing Methods

Our method is an optical sub-Nyquist sampling method that introduces optical delays across the channels. The key novelty of our work lies in constructing a frequency-domain covariance matrix where the subdiagonal terms generate a new vector $\beta(N)$. By applying a MUSIC scan over the folding index N , the algorithm jointly estimates frequency and DOA while naturally achieving parameter pairing. This design simplifies the hardware delay structure and reduces computational complexity, setting our approach apart from both electrical undersampling methods and existing optical methods.

Compared with electrical undersampling systems, our method demonstrates three distinct advantages: 1) a simpler delay structure, requiring only M delay channels instead of the $M \times P$ channels in [17], which greatly reduces hardware complexity; 2) more precise delay implementation, since optical fiber delay lines provide high accuracy and flexibility, whereas electronic systems depend on stringent ADC synchronization or low-precision electrical delay lines; and 3) better wideband adaptability, as electronic components are inherently narrowband, while optical devices naturally support tens-of-GHz analog bandwidth, making our system more advantageous for wideband signal measurements.

In optical measurement approaches, the frequency-power mapping method [22], [23], [25] features a simple architecture and strong instantaneous frequency measurement capability. However, this method is limited in handling wideband or multitone signals. In contrast, the frequency-time mapping method [24], [26] can achieve high-resolution frequency estimation, but its instantaneous bandwidth is relatively limited. In comparison with these two methods, frequency down-conversion-based measurement can be realized using an OFC, enabling wideband frequency characterization with improved precision and flexibility. Optical channelized receivers combine multiple OFCs to split the spectrum into subbands, but this is not an undersampling architecture. Dual-comb or multicomb undersampling methods down-convert signals

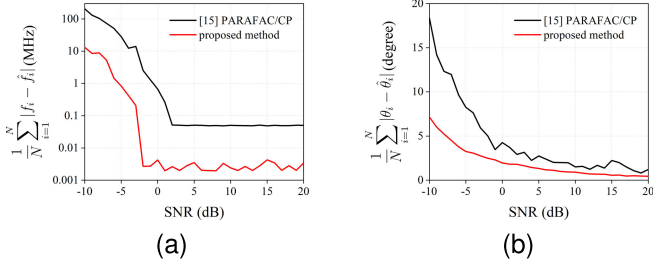


Fig. 4. Influence of SNR, with $M = 8$. (a) Frequency estimation performance. (b) DOA estimation performance.

into different frequency intervals but cannot exploit phase information for joint estimation. Other schemes [33], [34] rely on phase information for signal processing, but do not provide systematic algorithms for parameter estimation. By contrast, our approach differs fundamentally from existing OFC-based schemes, employing only one OFC with optical delays and leveraging the proposed covariance-matrix formulation. This enables accurate joint estimation with naturally paired frequency and angle results, while achieving lower system complexity and greater robustness.

IV. SIMULATION

In our simulation, we set $f_{\text{NYQ}} = 9.8$ GHz. The distance between two adjacent antennas is set to $d = 0.01$ m to meet the ambiguity-free requirement proposed in Section II, i.e. $d \leq \lambda_{\text{NYQ}}/2$.

Our carrier frequency is randomly selected from the range $[0, f_{\text{NYQ}}]$, and DOA is randomly chosen from $[0, 180^\circ]$. The simulated signal is constructed based on (1), and each signal path is independently corrupted by additive white Gaussian noise (AWGN). The performance of the parameter estimation algorithm is evaluated using the following formula:

$$\text{error}_f = \frac{1}{N} \sum_{i=1}^N |f_i - \hat{f}_i| \quad (28)$$

$$\text{error}_\theta = \frac{1}{N} \sum_{i=1}^N |\theta_i - \hat{\theta}_i|. \quad (29)$$

The first simulation tests the estimation performance of the algorithm as the SNR varies, comparing the performance differences between the PARAFAC/CP decomposition method in [15] and the proposed algorithm under different SNR conditions. We modified the CP-PASS-FD algorithm proposed in [15] to accommodate the optical delay under-sampling system, introducing a known delay between the OFC and the antennas instead of after the antennas. This adjustment allows for a direct comparison of the two algorithms performance within the same system framework. We set the number of snapshots in the simulation to 327 680, which is chosen as a compromise between computation time and estimation accuracy.

As shown in Fig. 4(a) and (b), our method exhibits significantly lower estimation errors in both carrier frequency and DOA, particularly under low-SNR conditions. To further illustrate this performance difference, we compare the average estimation errors under different SNR levels. For SNR values

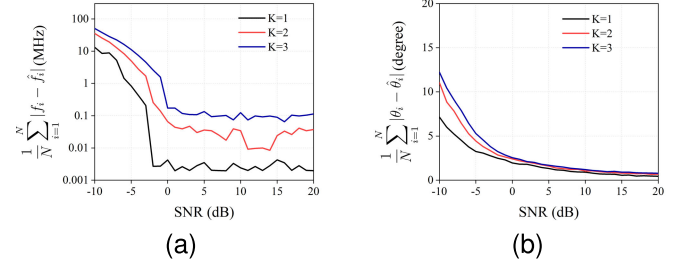


Fig. 5. Influence of different numbers of incident signals in the proposed method. (a) Frequency estimation performance. (b) DOA estimation performance.

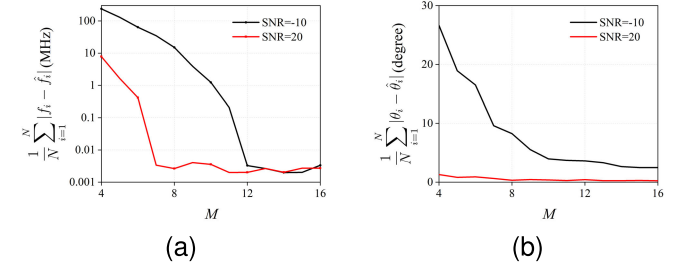


Fig. 6. Influence of array size M in the proposed method. (a) Frequency estimation performance. (b) DOA estimation performance.

greater than 0 dB, the frequency and DOA estimation errors remain around 3 kHz and 0.67° , respectively. In contrast, at an SNR of -10 dB, the errors increase to approximately 13 MHz and 8° , respectively.

The robustness of the proposed algorithm under low SNR conditions is attributed to the time-to-frequency domain transformation employed in the processing. This transformation allows coherent accumulation of signal energy, while noise being uniformly distributed in the frequency domain adds incoherently, effectively leading to an improvement in the SNR. Additionally, the CP decomposition method relies on randomly initialized matrices in the least-squares estimation process, which can significantly affect its performance under low SNR conditions. This may further explain its degraded accuracy in noisy environments. Overall, the proposed algorithm maintains high estimation accuracy even under low SNR, demonstrating superior adaptability for practical scenarios with limited signal quality.

To further evaluate the algorithm performance under multisignal conditions, simulations are conducted for $K = 1, 2$, and 3 incident signals. The carrier frequencies and DOAs are randomly selected within 0–9.8 GHz and 0° – 180° , respectively, and the error metrics followed (28) and (29). As shown in Fig. 5(a) and (b), both frequency and DOA estimation errors slightly increase with the number of incident signals K , mainly due to the baseband interference introduced by multiple tones. When $\text{SNR} > 10$ dB, the mean frequency and angular errors are approximately 30 kHz and 0.87° for $K = 2$, and 95 kHz and 0.94° for $K = 3$. These results indicate that the proposed method can still accurately estimate multiple parameters with only minor degradation in accuracy.

The third simulation evaluates the estimation performance of the carrier frequency and DOA with varying numbers of

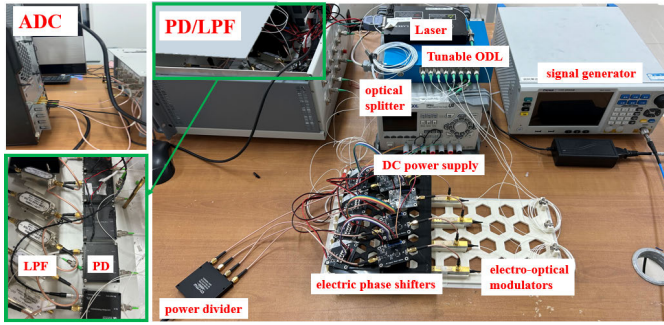


Fig. 7. Experimental photograph of the proposed system.

sensors M . We simulated the proposed algorithm performance with the number of sensors varying from 4 to 16, under SNR conditions of -10 and 20 dB. Fig. 6(a) and (b) shows that increasing the number of sensors enhances the system's robustness to noise, a benefit that is particularly noticeable at lower SNR levels.

V. EXPERIMENT

In this section, we describe the experiments to illustrate the performance of the proposed method for joint carrier frequency and DOA estimation.

A. Experiment Implementation

An experimental setup was designed to validate the proposed method, as shown in Fig. 7. An unknown RF signal was generated using a microwave signal generator (Siyi 1435D) and transmitted to a power splitter/divider (QY-PS4-2/18-SE). Each of the four output ports of the splitter was connected to an electric phase shifter to emulate the scenario in which signals arrive at the receiving antenna array from different DOAs. A pulse sampling sequence was generated by an OFC with a repetition rate of $f_0 = 206.385$ MHz. The optical pulses were split using a polarization-maintaining optical splitter and fed into four optical modulators via four optical delay lines (LT-MODL-4-15-PM-FA). The modulated optical signals were then detected by low-speed photodetectors. A low-pass filter was used to retain only the signals within the first frequency folding interval. An isolator was employed to protect the ADC, and the electrical signals were digitized and acquired using a four-channel ADC (M4i-4481, with up to 400 MSa/s per channel) for subsequent processing.

Given the fiber delay line lengths are set to [0, 50, 150, and 300 ps], the maximum measurable frequency is calculated to be 9906.5 MHz ($N_{\max} = 48$). Only the signals falling within the first repetition region $f_{\text{IF}} < f_0/2$ are considered. The sampling length is 327 680 points, which corresponds to a frequency resolution of 1.22 kHz under a 400 MSa/s sampling rate.

Due to the limitations of establishing far-field conditions, electric phase shifters were used to emulate the phase differences induced by far-field plane wavefronts. By applying controlled phase shifts between array elements according to theoretical models, the reception scenarios under different angles of arrival can be accurately replicated. The bandwidth of the phase discriminator was limited to 3–6 GHz, with each

phase shifter capable of adjusting the input signal phase $\Delta\varphi$ from 0° to 354.375° in 64 steps of 5.625° . By setting the equivalent element spacing to $d = 0.025$ m, θ can be calculated using the theoretical model derived from (3)

$$\Delta\varphi = \left(\frac{2\pi f_{\text{RF}} d \cos \theta}{c} \right). \quad (30)$$

B. Wideband Phase Calibration

Broadband calibration prior to the experiment is essential. The theoretical analysis is based on ideal conditions, assuming that, except for the optical delay lines, all other optical and electrical paths are of equal length and that all components exhibit identical responses. However, in practical measurements, mismatches in the lengths of optical and electrical paths, as well as inconsistencies in component responses, introduce time delays and phase distortions. These imperfections result in interference phase components that affect the phase information, thereby influencing both the matrix construction and the subsequent parameter estimation. We denote the total interference-induced phase shift as $\varphi(f)$, which can be decomposed into two main components as a function of two different delay times τ_1 and τ_2 .

- 1) A first component related to the RF frequency f_{RF} , denoted as $\varphi_{\text{RF}} = 2\pi N f_0 \tau_1$, which primarily results from path differences in the premodulation optical chain. Since each optical pulse samples the RF signal at different spatial positions, it introduces phase differences accordingly.
- 2) A second component related to the IF frequency f_{IF} , denoted as $\varphi_{\text{IF}} = 2\pi f_r \tau_2$, originates from differences in electrical path lengths or from linear phase discrepancies between channels in the post-modulation electrical chain. It should be noted that if the electrical components exhibit inconsistent and nonlinear phase responses across channels, the S_{21} phase response of each device should be measured with a vector network analyzer (VNA), and the resulting phase imbalance should be subtracted from the measured φ_{IF} . The delay τ_2 should then be determined from the slope of the phase curve after removing the electronic phase imbalance.

Therefore, the total phase shift in the system can be modeled as

$$\varphi(f) = 2\pi N f_0 \tau_1 + 2\pi f_r \tau_2 \quad (31)$$

where f_0 is the repetition frequency of the optical source, f_r is the IF frequency, and N is the frequency folding index. Given this relationship, the delay times τ_1 and τ_2 can be identified, for each working frequency f , thus enabling wideband phase calibration.

To calibrate the RF-related phase shift φ_{RF} , we first measure the optical delay τ_1 . According to the phase model, τ_1 leads to a phase shift linearly proportional to the folding index N . As illustrated in Fig. 8(a), RF signals are swept from 3 to 5.889 GHz in 206.385 MHz steps, corresponding to the repetition frequency f_0 . This ensures that all received signals share the same frequency offset f_r , and thus the IF-related phase φ_{IF} remains constant. The delay τ_1 can be estimated

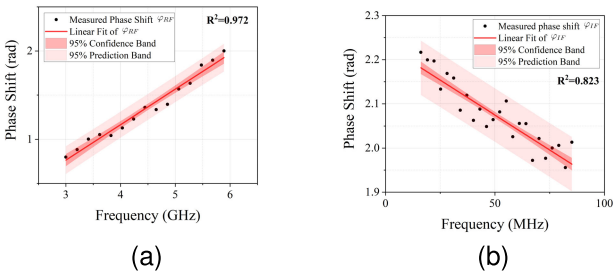


Fig. 8. Measured phase differences across wideband frequencies. (a) φ_{RF} . (b) φ_{IF} .

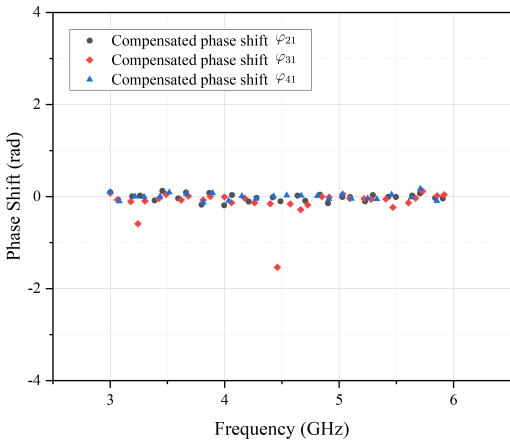


Fig. 9. Four-channel phase alignment results.

by fitting the measured phase data to a linear curve, with the slope yielding the delay.

For calibrating φ_{IF} , RF signals ranging from 4900 to 4970 MHz are swept in 1 MHz intervals and fed into the system, as shown in Fig. 8(b). In this frequency range, all received signals share the same folding index N , so the phase shift is only affected by f_r . Time delay τ_2 is extracted by curve fitting. The R^2 values (0.972 for RF and 0.823 for IF) confirm that the calibration maintains reliable linearity across both bands. Even though phase fluctuations arise in the IF band due to electronics-induced noise, the calibration maintains accurate and robust performance across the entire frequency range.

After obtaining the estimated parameters τ_1 and τ_2 , phase compensation can be performed by (31). For the RF-related phase term φ_{RF} , compensation is achieved by adjusting the optical delay line to correct τ_1 . In contrast, φ_{IF} depends only on τ_2 and the IF frequency f_r , and can thus be compensated directly using the term $2\pi f_r \tau_2$ once τ_2 is known. Fig. 9 presents the final compensated phase values across all four channels. The two outlier points of φ_{31} appear near the 0 and $f_0/2$ boundaries, where phase discontinuities make the measurements more sensitive to noise. These deviations are local and do not affect the overall calibration accuracy. In practice, any point showing large deviation can be regarded as a bad point and excluded during calibration to further improve robustness. The average residual phase error is approximately 0.06 rad, which remains well within the tolerance range of the proposed algorithm.

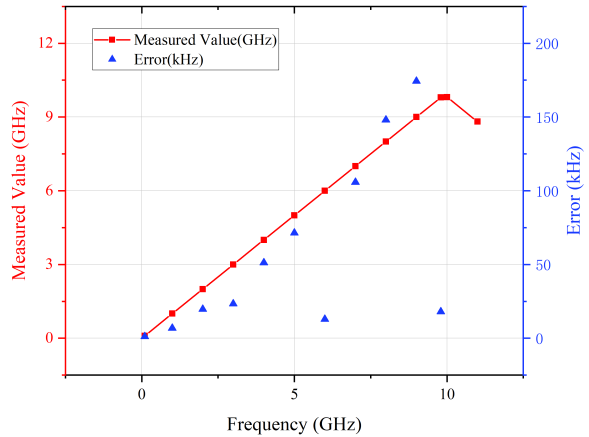


Fig. 10. Frequency measurement results and errors of the system.

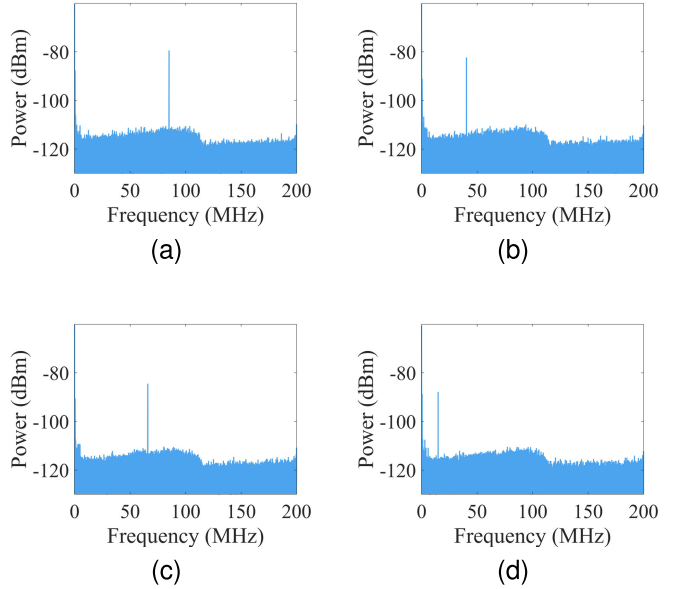


Fig. 11. Typical down-converted signals' spectrum with frequency at (a) 3.8 GHz, (b) 4.5 GHz, (c) 5.3 GHz, and (d) 6 GHz.

C. Frequency and DOA Estimation

First, we verify the system's ability to measure frequency. To evaluate the accuracy of the proposed method, we conducted 25 experiments across the frequency range of 100 to 11 000 MHz. Accuracy is defined in (28) and (29). The results of the frequency estimation and corresponding errors are illustrated in Fig. 10, where the red line indicates the frequency estimates, and the blue triangles represent the estimation errors.

Within the frequency range of 100–9800 MHz, the proposed system yields accurate results, with an average estimation error of approximately 50 kHz. To further verify the theoretical boundary condition derived in Section III-B, two additional measurements were performed at 10 000 and 11 000 MHz. As expected, the estimation becomes inaccurate once the input frequency exceeds the maximum measurable range (-9.9 GHz), confirming the validity of the theoretical limit.

Next, we evaluate the system's capability for joint estimation of carrier frequency and DOA. Five representative

TABLE II
ESTIMATED FREQUENCIES AND DOAs FOR INPUT SIGNALS

Image Sequence	Input Frequency (MHz)	Theoretical Phase (deg)	Theoretical DOA (deg)	Measured Frequency (MHz)	Measured DOA (deg)
a	3000	50.625	55.77	3000.023	57.24
b	3800	90.000	37.86	3800.019	35.52
c	4500	0.000	90.00	4499.997	90.21
d	5300	112.50	44.96	5300.005	44.96
e	6000	28.125	81.01	6000.013	81.07

TABLE III
ESTIMATION RESULTS FOR DUAL-TONE SIGNALS

Image Sequence	Input Frequency (MHz)	Theoretical Phase (deg)	Theoretical DOA (deg)	Measured Frequency (MHz)	Measured DOA (deg)
a	4999.99	0.00	90.0	4999.887	90.44
	5000.00	0.00	90.0	5000.008	90.53
b	3130.00	28.125	72.57	3130.019	70.90
	6000.00	28.125	81.01	6000.031	80.17
c	3250.00	45.00	62.51	3250.021	61.85
	4080.00	45.00	68.43	4080.014	68.66
d	4400.00	90.00	47.01	4400.000	46.70
	5400.00	90.00	56.25	5400.014	55.86

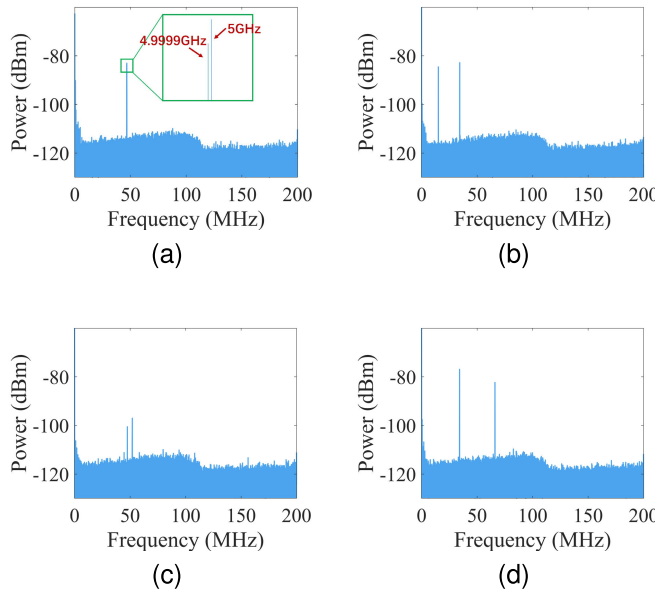


Fig. 12. Output power spectra of input two-tone signal with frequency at (a) 4.9999 and 5 GHz, (b) 3.13 and 6 GHz, (c) 3.25 and 4.08 GHz, and (d) 5.4 and 4.4 GHz.

frequency points, as listed in Table II, were selected for testing. The output power spectrum of typical down-converted signal is shown in Fig. 11. The third and fourth columns in Table II show the phase differences generated by the phase discriminator and theoretical DOA calculated by (30). The fifth and sixth columns present the estimated frequency and DOA values. The measurement errors primarily originate from the limited sampling length, the instability of the OFC repetition rate (several kHz), and the phase noise inherent in the system.

D. Dual-Tone Signal Estimation

Dual-tone signals composed of four different frequency combinations were tested, and their output power spectra are shown in Fig. 12. The first signal pair was used to evaluate the system's frequency resolution, which turned out to be 1.22 kHz in experimental practice. The remaining three signal pairs were measured with known phase offsets introduced through phase shifters. The experimental results are summarized in Table III.

Since the algorithm performs a preliminary estimation and separation of the signal distribution in the frequency domain, the system is capable of measuring multiple signals simultaneously, and its ability to distinguish signals with different frequencies is not constrained by the number of array elements. The frequency resolution of the system is jointly determined by the sampling rate and the finite sample length. Repeated measurements indicate that the system yields a DOA error of 0.7°, demonstrating high accuracy. Measurement errors arise from the limited sample length, the accuracy of the OFC repetition rate, and the system's random phase jitter.

E. Uncertainty Analysis

To quantify the reliability of the experimental results, an uncertainty evaluation is conducted, including both statistical and systematic contributions.

Type-A uncertainty is evaluated from repeated short-term measurements. For each frequency point j , the within-group standard deviation is given by

$$s_j = \sqrt{\frac{1}{n_j - 1} \sum_{i=1}^{n_j} (x_{ij} - \bar{x}_j)^2} \quad (32)$$

with x_{ij} denoting the i th measurement at frequency point j , \bar{x}_j the mean of the n_j measurements, and n_j the number of repetitions. Since this procedure relies on short-term

TABLE IV
COMPARISON WITH RECENT ELECTRICAL AND OPTICAL METHODS FOR FREQUENCY AND DOA ESTIMATION

Ref	Function	Method	Frequency Measurement Range (GHz)	Frequency Error	Multi-tone Support	DOA Measurement Range (degree)	DOA Error (degree)	complexity
[3]	Joint Frequency and DOA Estimation (Electrical)	Sub-Nyquist sampling	0–10	No experimental proof	Yes	$\pm 90^\circ$	No experimental proof	High
[4]			0–10		Yes	$\pm 90^\circ$		
[10]			0–10		Yes	$\pm 85^\circ$		
[15]			0–1		Yes	$\pm 90^\circ$		
[18]			0–10		Yes	$\pm 90^\circ$		
[22]	Frequency Measurement (Optical)	Frequency-power mapping	4.4–8.7	$\pm 200\text{MHz}$	No	N/A	N/A	Medium
[23]			7.5–20	100MHz	No			Medium
[24]		Frequency-time mapping	0–10	65MHz	Yes			Low
[29]		Optical sampling	1–20	1kHz	No			High
[31]			0–10	$\pm 25\text{kHz}$	Yes			Low
[32]			0–10	$\pm 25\text{kHz}$	Yes			Medium
[33]			1–12	N/A	Yes			Medium
[25]	Frequency and DOA Measurement (Optical)	Phase difference-amplitude mapping	0.5–36	$\pm 200\text{MHz}$	No	0–90°	$\pm 1^\circ$	Medium
[26]		Frequency-time mapping	11–17	8MHz	Yes	$\pm 69^\circ$	2.5°	Medium
[34]		Optical sampling	0.5–40	60kHz	Yes (power-based pairing)	$\pm 90^\circ$	1.8°	High
This work			0–9.8	50kHz	Yes (auto-pairing)	0–180°	0.7°	Medium

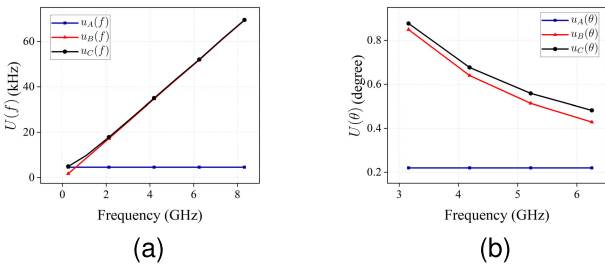


Fig. 13. Type-A, Type-B, and combined standard uncertainties. (a) Frequency estimation. (b) DOA estimation.

repeatability under stable conditions, the evaluated Type-A uncertainty can be considered independent of the operating frequency. Consequently, the pooled standard deviation is used to represent the overall Type-A uncertainty across multiple frequency groups, and is calculated as

$$u_A = \sqrt{\frac{\sum_j (n_j - 1) s_j^2}{\sum_j (n_j - 1)}} \quad (33)$$

Type-B uncertainty is obtained from specification-level parameters and model-based propagation. For frequency estimation, the dominant contributions are the repetition rate jitter

of OFC, denoted as δf_0 , and the FFT grid quantization error, denoted as δf_{FFT} . Assuming these two sources are independent, the total variance is the sum of their variances. The frequency error model is therefore expressed as

$$\delta f = |N| \delta f_0 + \delta f_{\text{FFT}} \quad (34)$$

where N is the folding index. Accordingly, the Type-B standard uncertainty of frequency estimation is given by

$$u_B(\hat{f}) = \sqrt{N^2 u^2(f_0) + u^2(f_{\text{FFT}})} \quad (35)$$

with $u(f_0)$ the standard uncertainty of the comb repetition rate and $u(f_{\text{FFT}})$ the standard uncertainty associated with the FFT frequency resolution.

For DOA estimation, the dominant Type-B contributions arise from the residual phase error after calibration and the propagation of frequency estimation inaccuracy. Accordingly, the Type-B uncertainty of DOA is obtained by standard error propagation as

$$u_B^2(\hat{\theta}) = \left(\frac{\partial \theta}{\partial \phi} \right)^2 u^2(\phi) + \left(\frac{\partial \theta}{\partial f} \right)^2 u_B^2(\hat{f}) \quad (36)$$

where $u(\phi)$ is the standard uncertainty of the residual phase. The sensitivity coefficients are

$$\frac{\partial \theta}{\partial \phi} = \frac{c}{2\pi f d \sin \theta} \quad \frac{\partial \theta}{\partial f} = \frac{c\phi}{2\pi d f^2 \sin \theta}. \quad (37)$$

Finally, the overall combined standard uncertainty is

$$u_c = \sqrt{u_A^2 + u_B^2} \quad (38)$$

Fig. 13 presents the uncertainty curves, where the Type-A uncertainty is evaluated from repeated experimental measurements, and the Type-B uncertainty is obtained from Monte Carlo simulations. It can be observed that the frequency uncertainty increases with frequency, which results from the linear amplification effect of the folding index N , consistent with the theoretical expression in (34). In contrast, the DOA uncertainty decreases with increasing frequency. This is because at lower frequencies, even a small residual phase uncertainty $u(\phi)$ leads to large angular fluctuations due to the high sensitivity $\partial\theta/\partial\phi$; whereas at higher frequencies this sensitivity decreases significantly, resulting in a reduced DOA uncertainty, in agreement with (36) and (37). In summary, the observed trends of frequency and DOA uncertainties are consistent with the theoretical sensitivity analysis, confirming the validity of the proposed uncertainty model.

F. Comparison and Discussion

Table IV summarizes and compares various frequency and DOA measurement schemes. It can be observed that sub-Nyquist receiver architectures are capable of estimating both multitone frequencies and directions of arrival. However, due to the high implementation complexity of such systems, some works only provide simulation results without experimental validation. As for microwave photonic approaches, such as frequency-time mapping and frequency-power mapping methods, they usually exhibit estimation errors on the order of tens of megahertz. In contrast, optical sampling schemes offer lower estimation errors, broader measurement ranges, and simpler implementations, representing key advantages for high-precision frequency and DOA measurements.

It should be noted that the experimental setup in this work emulates the far-field condition through electrical signal injection, which ensures that the investigation of algorithmic performance is not affected by external environmental factors. In particular, factors such as: 1) antenna position mismatch; 2) multipath interference; and 3) environment-induced phase instability are not included in the present experimental validation. In future work, we will further conduct experiments under practical antenna deployment and multipath propagation conditions to evaluate the practicality of the proposed method in nonideal environments.

VI. CONCLUSION

In this article, we proposed a low-complexity, high-resolution receiver architecture for joint frequency and DOA estimation of multiband signals, leveraging a single OFC and a linear array structure with optical delays. The proposed system exhibits notable advantages, including hardware simplicity, strong noise robustness, and excellent wideband adaptability. Furthermore, the jointly designed frequency and DOA estimation algorithm effectively addresses the challenges

of frequency ambiguity and parameter matching in other OFC systems, significantly reducing computational complexity and improving identification accuracy. Both simulations and experiments validate the feasibility and performance of the proposed approach.

We will further conduct research on more complex scenarios, including situations where unknown wideband signals are folded or aliased after under-sampling.

REFERENCES

- [1] M. Mishali and Y. C. Eldar, "Blind multiband signal reconstruction: Compressed sensing for analog signals," *IEEE Trans. Signal Process.*, vol. 57, no. 3, pp. 993–1009, Mar. 2009.
- [2] M. Mishali and Y. C. Eldar, "From theory to practice: Sub-Nyquist sampling of sparse wideband analog signals," *IEEE J. Sel. Topics Signal Process.*, vol. 4, no. 2, pp. 375–391, Apr. 2010.
- [3] S. Jiang, N. Fu, Z. Wei, X. Li, L. Qiao, and X. Peng, "Joint spectrum, carrier, and DOA estimation with beamforming MWC sampling system," *IEEE Trans. Instrum. Meas.*, vol. 71, pp. 1–15, 2022.
- [4] S. Jiang, N. Fu, Z. Wei, Z. Lian, L. Qiao, and X. Peng, "Compressed sampling for spectrum measurement and DOA estimation with array cooperative MWC," *IEEE Trans. Instrum. Meas.*, vol. 72, pp. 1–14, 2023.
- [5] R. Schmidt, "Multiple emitter location and signal parameter estimation," *IEEE Trans. Antennas Propag.*, vol. AP-34, no. 3, pp. 276–280, Mar. 1986.
- [6] T. Kailath, "ESPRIT-estimation of signal parameters via rotational invariance techniques," *Opt. Eng.*, vol. 29, no. 4, p. 296, Apr. 1990.
- [7] D. Malioutov, M. Çetin, and A. S. Willsky, "A sparse signal reconstruction perspective for source localization with sensor arrays," *IEEE Trans. Signal Process.*, vol. 53, no. 8, pp. 3010–3022, Aug. 2005.
- [8] J. Dai, N. Hu, W. Xu, and C. Chang, "Sparse Bayesian learning for DOA estimation with mutual coupling," *Sensors*, vol. 15, no. 10, pp. 26267–26280, 2015.
- [9] S. Wang et al., "A robust direction-of-arrival (DOA) estimator for weak targets based on a dimension-reduced matrix filter with deep nulling and multiple-measurement-vector orthogonal matching pursuit," *Remote Sens.*, vol. 17, no. 3, p. 477, Jan. 2025.
- [10] S. Stein Ioushua, O. Yair, D. Cohen, and Y. C. Eldar, "CaSCADE: Compressed carrier and DOA estimation," *IEEE Trans. Signal Process.*, vol. 65, no. 10, pp. 2645–2658, May 2017.
- [11] S. Stein, O. Yair, D. Cohen, and Y. C. Eldar, "Joint spectrum sensing and direction of arrival recovery from sub-nyquist samples," in *Proc. IEEE 16th Int. Workshop Signal Process. Adv. Wireless Commun. (SPAWC)*, Jun. 2015, pp. 331–335.
- [12] B. Liang, Q. Xu, C. Wang, and Y. Gao, "A low complexity mixed-field sources parameter estimation framework at sub-nyquist sampling rates," in *Proc. Int. Wireless Commun. Mobile Comput. (IWCMC)*, Jun. 2023, pp. 1046–1051.
- [13] L. Yang and Y. Han, "A joint spatio-temporal sub-nyquist sampling structure for wideband receivers," *IEEE Trans. Instrum. Meas.*, vol. 73, pp. 1–15, 2024.
- [14] A. Anil Kumar, S. G. Razul, and C.-M.-S. See, "Spectrum blind reconstruction and direction of arrival estimation of multi-band signals at sub-nyquist sampling rates," *Multidimensional Syst. Signal Process.*, vol. 29, no. 2, pp. 643–669, Apr. 2018.
- [15] F. Wang, J. Fang, H. Duan, and H. Li, "Phased-array-based sub-nyquist sampling for joint wideband spectrum sensing and direction-of-arrival estimation," *IEEE Trans. Signal Process.*, vol. 66, no. 23, pp. 6110–6123, Dec. 2018.
- [16] L. Liu, J.-F. Gu, and P. Wei, "Joint DOA and frequency estimation with sub-nyquist sampling," *Signal Process.*, vol. 154, pp. 87–96, Jan. 2019.
- [17] A. A. Kumar, S. G. Razul, M. G. Chandra, C. M. See, and P. Balamuralidhar, "Joint frequency and direction of arrival estimation with space-time array," in *Proc. IEEE Sensor Array Multichannel Signal Process. Workshop (SAM)*, Jul. 2016, pp. 1–5.
- [18] L. Liu, Z. Zhang, X. Zhang, P. Wei, J. An, and H. Li, "Joint spectrum sensing and DOA estimation based on a resource-efficient sub-nyquist array receiver," *IEEE Trans. Signal Process.*, vol. 72, pp. 5354–5370, 2024.
- [19] X. Zou, B. Lu, W. Pan, L. Yan, A. Stöhr, and J. Yao, "Photonics for microwave measurements," *Laser Photon. Rev.*, vol. 10, no. 5, pp. 711–734, Sep. 2016.

- [20] Y. Bai et al., "Microwave photonic links and transversal microwave photonic applications," *Electromagn. Sci.*, vol. 3, no. 1, pp. 0090541–1, 2025.
- [21] Y. Xie et al., "Applications of quantum dash mode-locked laser in microwave photonics," *Electromagn. Sci.*, vol. 3, no. 1, pp. 1–16, Mar. 2025.
- [22] J. Li, L. Pei, T. Ning, J. Zheng, Y. Li, and R. He, "Measurement of instantaneous microwave frequency by optical power monitoring based on polarization interference," *J. Lightw. Technol.*, vol. 38, no. 8, pp. 2285–2291, Apr. 15, 2020.
- [23] G. Wang et al., "Instantaneous frequency measurement with full FSR range and optimized estimation error," *J. Lightw. Technol.*, vol. 40, no. 18, pp. 6123–6130, Sep. 16, 2022.
- [24] S. Zhang, Y. Yang, S. Xie, and Y. Tian, "A segment match-filtering method based on microwave photonic frequency-time mapping," *IEEE Trans. Instrum. Meas.*, vol. 73, pp. 1–9, 2024.
- [25] R. Wang, Y. Fan, W. Zhai, J. Tan, X. Pang, and Y. Gao, "A simple approach for simultaneous measurement of instantaneous frequency and angle of arrival," *IEEE Trans. Instrum. Meas.*, vol. 73, pp. 1–8, 2024.
- [26] X. Zhang, S. Yang, B. Yang, Y. Gao, H. He, and H. Chi, "Simultaneous measurement of AOA and frequency based on stimulated Brillouin scattering and frequency-to-time mapping," *J. Lightw. Technol.*, vol. 42, no. 16, pp. 5606–5615, Aug. 16, 2024.
- [27] T. Yasui et al., "Real-time absolute frequency measurement of continuous-wave terahertz radiation based on dual terahertz combs of photocarriers with different frequency spacings," *Opt. Exp.*, vol. 23, no. 9, pp. 11367–11377, 2015.
- [28] X. Zhao, C. Li, Y. Pan, G. Hu, T. Yasui, and Z. Zheng, "Dual-comb-assisted real-time microwave frequency measurement with a single mode-locked fiber laser," in *Proc. Conf. Lasers Electro-Optics (CLEO)*, Jun. 2016, pp. 1–2.
- [29] X. Zhao et al., "Dead-band-free, high-resolution microwave frequency measurement using a free-running triple-comb fiber laser," *IEEE J. Sel. Topics Quantum Electron.*, vol. 24, no. 3, pp. 1–8, May 2018.
- [30] M. S. Alshaykh, D. E. Laird, J. D. McKinney, and A. M. Weiner, "Rapid wideband RF subsampling and disambiguation using dual combs," in *Proc. Conf. Lasers Electro-Optics (CLEO)*, 2019, pp. 1–2.
- [31] Y. Yang, S. Xie, Y. Dong, T. Wang, and X. Zhao, "A frequency recovering method for photonic under-sampling E-field measurement," *IEEE Sensors J.*, vol. 21, no. 12, pp. 13495–13505, Jun. 2021.
- [32] Y. Yang, S. Xie, T. Wang, Y. Dong, X. Zhao, and M. Yang, "Multi-frequency electric field measurement method for optical under-sampling system," *IEEE Sensors J.*, vol. 21, no. 20, pp. 23024–23036, Oct. 2021.
- [33] T. Wang, Y. Yang, S. Xie, S. Luan, and Y. Li, "Frequency-phase-mapping method in microwave frequency measurement with single optical frequency comb," *IEEE Sensors J.*, vol. 24, no. 8, pp. 12616–12623, Apr. 2024.
- [34] X. Li, A. Wen, X. Li, and Y. Yang, "Wideband frequency and angle-of-arrival measurement system based on optical subsampling," *IEEE Trans. Microw. Theory Techn.*, vol. 71, no. 2, pp. 784–794, Feb. 2023.